Proceedings of IMECE2008
2008 ASME International Mechanical Engineering Congress and Exposition
October-November 31-6, 2008, Boston, MA USA

IMECE2008-67553

STATIC AND DYNAMIC ANALYSIS OF A BISTABLE MICRO-ACTUATOR

S. Towfighian
Mechanical Engineering
University of Waterloo
Waterloo, ON N2L 3G1, Canada
Email: stowfigh@engmail.uwaterloo.ca

E. M. Abdel-Rahman*
Systems Design Engineering
University of Waterloo
Waterloo, ON N2L 3G1, Canada
Email: eihab@engmail.uwaterloo.ca

G. R. Heppler
Systems Design Engineering
University of Waterloo
Waterloo, ON N2L 3G1, Canada
Email: heppler@uwaterloo.ca

ABSTRACT

The static response of an electrostatic micro-catilever beam has been obtained by using Galerkin's method. To make the system bi-stable, a controller has been added and the static response profile is presented using a multi-mode model for the beam. The number of mode shapes leading to convergence has been studied. The softening effect of adding more mode shapes has been investigated along with the effect of changing the system parameters on the static response. Decreasing the controller gain has been found to widen the voltage range of the bi-stability region and increasing the sensor amplification factor is shown to push the upper equilibrium point away from pull-in. Properly choosing these parameters can adjust the range of voltage for bi-stability. By doing a linearization about the stable fixed points, we also found the two natural frequencies for each stable equilibrium point. Finally, we have found the dynamic response of the bi-stable system using one- and three-mode-models. The basins of attraction for each stable fixed point and the exchange of energy between the two potential energy wells(equilibrium points), are demonstrated.

1 Introduction

Nonlinearities in MEMS devices have been studied over a decade for different applications. For micro-structures in electrostatic fields a nonlinearity exists because of electrostatic loading, which leads to chaos in some electrostatic resonators [1–3]. The simulations have been based on a lumped parameter system model. In 1998, Bienstman et al. [1] developed an autonomous impact resonator by taking advantage of the hard-spring effect and pull-in present in a microbridge electrostatic resonator. They observed periodic behaviour as well as chaotic behaviour in the system response. Their system is a microbridge that uses electrostatic excitation and impact to operate the resonator without the need for a separate control circuit. The microbridge resonator acts as an electrode in a capacitor that is driven at a voltage larger than the pull in voltage, forcing it to collapse. Thereby, a short circuit happens that results in capacitor discharge and oscillation of the beam; the charge gradually builds up causing pull in and the impact happens again. Therefore, the resonator oscillation is autonomous in the system and there is no external exciation. They observed chaos for certain parameters of the system in the simulations and period doubling in the experiments.

Wang et al. [2] modelled and characterized a nonlinear MEMS oscillator consisting of parallel-reduction comb drives acting as the electrostatic tuning actuator. The system acts as a Duffing oscillator with a two-well potential field. They obtained chaos by selecting suitable tuning voltages and damping. In the Duffing equation, the applied electrical force contributes to both the forcing function and the effective stiffness of the system. Through simulation and experiments, they have shown period doubling, period three, and chaotic oscillations for the bistable region of the system. They proposed to benefit from synchronized chaos for secure communication.

Raman et al. [3] reported chaos in atomic force microscopy. They observed and characterized weak chaos in microcantilever beams with nanoscale tips under variety of operating conditions. The observed chaos was "weak", conaining strong periodic oscillation that could create fundamental limits on nanometrology.

*Address all correspondence to this author.

Pull-in instability, another nonlinear phenomenon in MEMS under electrostatic loading, has also been investigated. Pull-in happens when the balance between elastic and electrical forces is lost and the system becomes unstable. Zhang et al. [4] obtained the critical pull-in deflection for micro-beams with different boundary conditions. They analyzed a continuous model for the beam, but assumed that the first mode shape is the dominant defelction shape and only the first mode shape is used for discretization. In other papers [5,6], the pull-in point is obtained for lumped model of spring, mass, damper systems.

Here, we find the pull-in instability profile of a micro cantilever beam under electrostatic loading using a continuous model for the beam. The distributed parameter equation of motion of the beam is then discretized using Galerkin's method with the mode shapes of a cantilever beam. Applying the reduced–order model proposed by Yonnis et al. [7] for the elctrostatic force, the equations became easier to simulate that still account for the coupling between the mechanical and electrical forces. We investigate here the number of modes required to obtain convegence for the static defelction of the beam (pull-in profile) in the elctrostatic field. The beam dimensions are based on the those used by Liu et al. [6].

In order to create chaos in the system, the control law introduced by Liu [6] is used. The beam has one stable and one unstable equilibrium points for most of its operating voltage without the controller. The proposed controller adds one more stable equilibrium point for a limited operating voltage which makes the system bistable. The static profile of the system after adding the controller is obtained for the finite degree of freedom system of the cantilever beam. The effect of considering a higher number of mode shapes is studied here. In addition, the dynamic response of the system is obtained for the model and the creation of chaos is investigated.

2 System Modeling

The equation of motion of a cantilever beam in an electrostatic field in the presence of some damping (Figure 1), becomes

$$\rho A\frac{\partial^2\hat{w}(\hat{x},\hat{t})}{\partial\hat{t}^2}+EI\frac{\partial^4\hat{w}(\hat{x},\hat{t})}{\partial\hat{x}^4}+c\frac{\partial\hat{w}(\hat{x},\hat{t})}{\partial t}=\frac{\varepsilon bV_{DC}^2}{2(d-\hat{w}(\hat{x},\hat{t}))^2} \quad (1)$$

where $\hat{w}(\hat{x},\hat{t})$ is the deflection of the beam in the $\hat{z}$ direction, $\hat{x}$ is the coordinate along the beam length, and $\hat{t}$ is time. V_{DC} is the applied DC voltage and other parameters are defined in Table 1. In order to make the computation procedure easier, the method of multiplying both sides by $(d-\hat{w})^2$ [7] is used, hence

$$\rho A\frac{\partial^2\hat{w}}{\partial\hat{t}^2}(d-\hat{w})^2+EI\frac{\partial^4\hat{w}}{\partial\hat{x}^4}(d-\hat{w})^2+c\frac{\partial\hat{w}}{\partial\hat{t}}(d-\hat{w})^2=\frac{\varepsilon bV_{DC}^2}{2} \quad (2)$$

For improving the accuracy in the numerical solution of Eq. (2), the following non-dimensional parameters are introduced

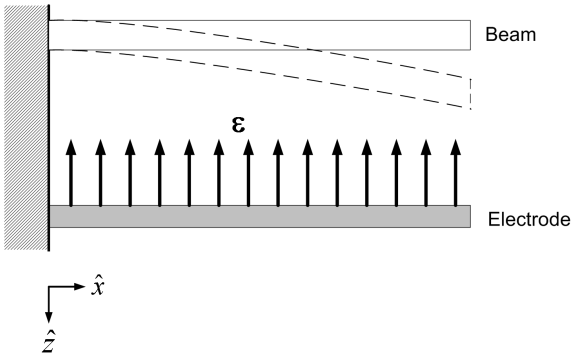

Figure 1: Schematic of microbeam oscillator.

$$x=\frac{\hat{x}}{L},\quad w=\frac{\hat{w}}{d},\quad t=\frac{\hat{t}}{T} \quad (3)$$

where

Table 1: Actuator and controller parameters [6]

Parameter	**Symbol**	**Value**
Sensor system parameter	Ψ	1.5274 V
Controller gain	G	1
Density	ρ	2331 $\frac{kg}{m^3}$
Beam Length	L	200 μm
Beam Width	b	80 μm
Beam height	h	4.5 μm
Initial gap	d	3 μm
Damping coefficient	μ	0.73
Permittivity of free space	ε_0	8.85E-12 $\frac{F}{m}$
Modulus of Elasticity	E	166 GPa
Bandwidth of the low pass filter	r	1

$$T=\sqrt{\frac{\rho AL^4}{EI}}. \quad (4)$$

Substituting the above parameters in Eq. (2) and simplifying results in

$$\frac{\partial^2 w}{\partial t^2}(1-w)^2+\frac{\partial^4 w}{\partial x^4}(1-w)^2+\mu\frac{\partial w}{\partial t}(1-w)^2=\alpha V_{DC}^2 \quad (5)$$

where we have introduced the parameters

$$\mu = \frac{cL^4}{EIT} \quad \text{and} \quad \alpha = \frac{\varepsilon b L^4}{2EId^3} \tag{6}$$

Two initial conditions and four boundary conditions are needed for finding a unique solution for $w(x,t)$. The boundary conditions are those for a cantilever beam and are

$$w\big|_{x=0} = 0, \quad \frac{\partial w}{\partial x}\big|_{x=0} = 0,$$
$$M\big|_{x=1} = EI\frac{\partial^2 w}{\partial x^2}\Big|_{x=1} = 0, \quad V\big|_{x=1} = EI\frac{\partial^3 w}{\partial x^3}\Big|_{x=1} = 0 \tag{7}$$

A solution to Eq. (5) will be sought by using Galerkin's method with a trial function of the form

$$w(x,t) = \sum_n \Phi_n(x) q_n(t). \tag{8}$$

where $x = 1$ corresponds to the beam tip. The frequency equation for the boundary conditions of Eq. (7) is

$$1 + \cosh(\beta)\cos(\beta) = 0 \tag{9}$$

There are an infinite number of β, that satisfy Eq. (9). They will be denoted as $\beta_n, \quad n = 1, 2, \cdots$, where n is the mode shape number. The corresponding Φ_n is then of the form

$$\Phi_n(x) = A_n\{\sin(\beta_n x) - \sinh(\beta_n x) + \gamma_n[\cos(\beta_n x) - \cosh(\beta_n x)]\} \tag{10}$$

where

$$\gamma_n = -\frac{\sin(\beta_n) + \sinh(\beta_n)}{\cos(\beta_n) + \cosh(\beta_n)} \tag{11}$$

and A_n is an arbitrary constant, and is chosen to get mode shapes normalized with respect to the beam tip modal deflection, Φ_{n1}, i.e.

$$A_n = \frac{1}{\Phi_{n1}} = \frac{1}{\sin(\beta_n) - \sinh(\beta_n) + \gamma_n[\cos(\beta_n) - \cosh(\beta_n)]} \tag{12}$$

Therefore, the specific form of the trial function, Eq. (8), is

$$w(x,t) = \sum_{n=1}^{M} \Phi_n(x) q_n(t) \tag{13}$$

where M is the number of modes (degrees of freedom) considered in the expansion. Eq. (13) is then used in Eq. (5) to get

$$\sum_{n=1}^{M} \Phi_n(x)\ddot{q}_n(t)(1 - \sum_{n=1}^{M} \Phi_n(x) q_n(t))^2$$
$$+ \sum_{n=1}^{M} \Phi_n^{(4)}(x) q_n(t)(1 - \sum_{n=1}^{M} \Phi_n(x) q_n(t))^2$$
$$+ \mu \sum_{n=1}^{M} \Phi_n(x)\dot{q}_n(t)(1 - \sum_{n=1}^{M} \Phi_n(x) q_n(t))^2 = \alpha V_{DC}^2 \tag{14}$$

where $\Phi_n^{(4)}(x)$ is the fourth derivative of Φ_n with respect to x. The Galerkin method is then used; multiplying both sides of Eq. (14) by the normalized mode shapes $\Phi_i(x)$, integrating from $x = 0$ to $x = 1$, and using the orthogonality condition:

$$\int_0^1 \Phi_i(x)\Phi_n(x)dx = \kappa_i \delta_{ij} \tag{15}$$

where δ_{ij} is the Kronecker delta. The resulting equation after employing the Galerkin method, is a set of M ordinary second order differential equations in terms of q_n where $i = 1 \cdots M$.

2.1 Static Analysis

The equilibrium equation for the cantilever beam is the balance between the electrostatic force and the elastic force. When this balance is lost, the system becomes unstable. When the elastic force can not resist the electrostatic force the bottom electrode pull-in the above electrode (beam) and stability is lost, this is called the pull-in point. In this section, the static equilibrium of the beam is studied. The equilibrium points of the system are found at different applied voltages in the electrostatic field. The equilibrium equation is obtained from the equation of motion of Eq. (14) in the steady state condition, where $\ddot{q}_n = 0$, $\dot{q}_n = 0$, such that

$$\sum_{n=1}^{M} \Phi_n^{(4)}(x) q_n(t)\Big(1 - \sum_{n=1}^{M} \Phi_n(x) q_n(t)\Big)^2 = \alpha V_{DC}^2 \tag{16}$$

Galerkin's method is then applied. The result is a set of cubic polynomial equations in terms of q_n for $n = 1 \cdots M$ and their products, the solution of which is obtained for an assumed applied voltage V_{DC}. Having solved for each q_n, the beam tip deflection is then found from

$$w_1 = w\big|_{x=1,t} = \sum_{n=1}^{M} \Phi_n\big|_{x=1} q_n(t) = \sum_{n=1}^{M} q_n(t) \tag{17}$$

The number of modes that leads to a convergent solution is investigated below. For a one mode approximation, the equilibrium equation for the beam tip deflection is

$$\omega_1^2 q_1 + c_2 q_1^2 + c_3 q_1^3 = \alpha_0 V_{DC}^2 \tag{18}$$

where ω_1 is the first natural frequency of the beam, c_2, c_3, and α_0 are found after applying Galerkin's method. For the first mode approximation, the beam tip deflection, $w_1 = q_1$.

The solution to the algebric Eq. (18) is found numerically at each voltage, V_{DC}. Figure 2 shows the pull-in graph for Eq. (18) for one mode as well as the results for up to six modes. The graph demonstrates the nondimensional beam tip deflection versus applied DC voltage. The point on the graph where the slope of deflection versus voltage becomes infinite is the pull-in point which means that small changes of the voltage around this point

makes the rate of change of the deflection infinity and causes failure. That is when the beam deflection drastically increases until breakage happens. The pull in deflection is found to be at 45 percent of the gap between the electrode and the beam for the continuous model of the actuator, which is higher than 33 percent of the gap predicted using a single DOF system [4].

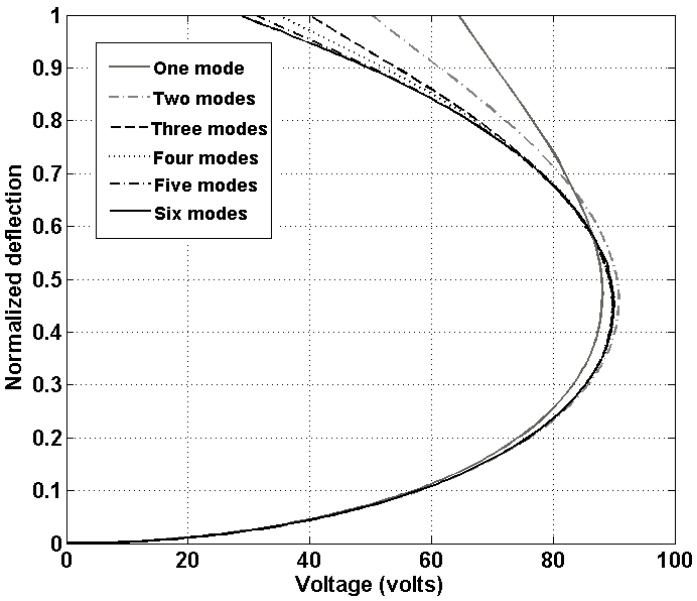

Figure 2: Nondimensional deflection of the beam tip versus voltage.

The lower branch below the pull-in point in Figure 2 represents a locus of stable equilibrium points at a specified voltage, while the upper branch is a locus of the unstable equilibrium points. The lower branch converges assuming the first three mode shapes, though the upper branch shows convergence only on some part. Increasing the number of modes in the equations stretches the length along which the solution converges and delays divergence. In addition, the fewer the number of modes used in Eq. 16, the earlier the system crosses $w = 1$, the gap distance.

3 Modeling of System and Controller

A controller [6] is added to the micro-actuator in order to create a bi-stable system (Figure 3). By adding the controller, the equation of motion in terms of the normalized deflection w changes to

$$\ddot{w}(1-w)^2 + w^{(4)}(1-w)^2 + \mu\dot{w}(1-w)^2 = G^2(V_r - V_s)^2 \quad (19)$$

where V_s is the output of the sensor, G is the controller gain ,and V_r is the normalized reference input voltage of the actuator

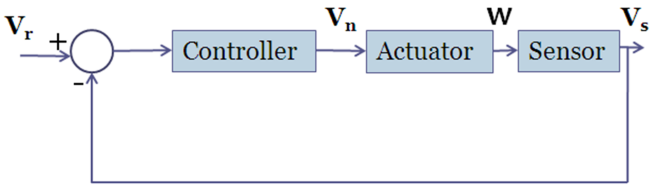

Figure 3: Controller and sensor system (adopted from [6]).

$$V_r = V_{ref}\sqrt{\alpha} \quad (20)$$

where V_{ref} is the reference input voltage. The controller [6] adds another equation to the system, which is

$$\dot{V}_s = -r\Big(V_s - \frac{w_1}{1-w_1}\Psi\sqrt{\alpha}\Big) \quad (21)$$

where w_1 is the normalized deflection of the beam tip and

$$\Psi = \frac{K_s V_{mod}}{\frac{dC_c}{\varepsilon_0 bL} - 1} \quad (22)$$

where K_s is the gain of the sensor amplifier, and V_{mod} is the input to the sensor amplifier defined by Liu [6]. The bandwidth of the low pass filter placed after the sensor in the closed loop system is denoted by r, and C_c is the parasitic capacitance of the closed loop system.

3.1 Static Analysis with Controller

The static response of the system after adding the controller is investigated below. The response is the balance between the controller and elastic forces. Previously the system itself had only one stable equilibrium point. Adding the controller creates one more stable equilibrium point, making the system bi-stable for a limited range of operating voltage. For drawing the static profile, Eqs. (19) and (21) are solved by equating the derivatives with respect to time to zero. Subsequently, from Eq. (21) V_s is then found to be

$$V_s = \frac{w_1}{1-w_1}\Psi\sqrt{\alpha} \quad (23)$$

Equation (23) is substituted into Eq. (19) with zero time derivatives and yields

$$w^{(4)}(1-w)^2 = G^2\alpha\Big(V_{ref} - \frac{w_1}{1-w_1}\Psi\Big)^2 \quad (24)$$

Using Eqs. (13) and (17) in Eq. (24) and simplifying, results in

$$\Big(\sum_{n=1}^{M}\Phi_n^{(4)}q_n\Big)\Big(1-\sum_{n=1}^{M}\Phi_n q_n\Big)^2\Big(1-\sum_{n=1}^{M}q_n\Big)^2 = G^2\alpha\Big[V_{ref}\Big(1-\sum_{n=1}^{M}q_n\Big) - \Psi\sum_{n=1}^{M}q_n\Big]^2 \quad (25)$$

The above equation is treated by means of Galerkin's method using the Φ_n from Eq. (10). The result is a set of quintic polynomial equations in terms of q_n for $n = 1 \cdots M$ and their products. For example, using a one mode approximation, the equation to solve for q_1 is

$$q_1^5 + a_4 q_1^4 + a_3 q_1^3 + f_2(V,G) q_1^2 + f_1(V,G) q_1 + f_0(V,G) = 0 \quad (26)$$

where $V = V_{ref}$ and the $f_n(V,G)$ are

$$\begin{aligned} f_2(V,G) &= c_0 + G^2 \left(c_1 V + c_2 V^2 + c_3\right) \\ f_1(V,G) &= d_0 + G^2 \left(d_1 V + d_2 V^2 + d_3\right) \\ f_0(V,G) &= e_0 G^2 V^2, \end{aligned} \quad (27)$$

and all other constants are obtained from Galerkin's formulation. The solution of Eq. (26) is sought at different voltages V. The system parameters used in the simulations are based on the system in reference [6] as listed in Table 1. The results are found numerically.

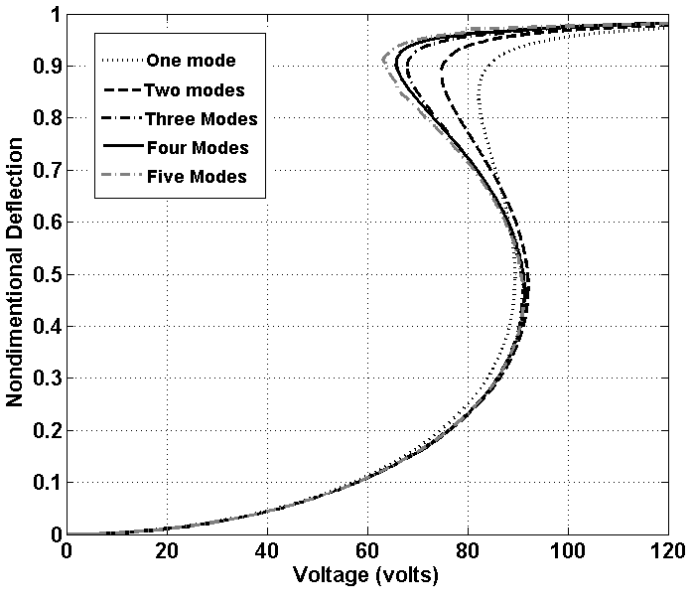

Figure 4: Normalized deflection of the beam tip after adding the controller.

Figure 4 depicts the nondimensional beam tip deflection versus volatge results for one to five modes. The profile has two turning points, which have infinite slopes, and in fact are saddle-node bifurcation points. Once we increase the voltage, at the first turning point, the one fixed point becomes two and then three and at the second turning point, the number of fixed points decreases to two and then it becomes one afterwards showing saddle-node bifurcation. The stability of the fixed points is investigated in section 4.1. As may be seen in the figure and from the stability analysis of section 4.1, the system has one lower stable equilibrium point for voltages lower than 65 V and one upper stable equilibrium point for voltages higher than 90 V. For the volatges between about 65 and 90 V, there is one upper and one lower stable equilibrium point and one middle unstable equilibrium point. Increasing the number of mode shapes not only widens the range of voltage for bi-stability, but it also make the first bifurcation happen at lower voltage. At a specified voltage in the bistability region, the upper equilibrium point is larger for a higher number of modes, meaning that for a certain amount of forcing, models with more modes deflect more (softening effect). Similarly, for a certain deflection amount e.g. 0.85, models with fewer modes need more voltage. This effect shows the added flexibility to the system model by using more mode shapes.

In order to discuss the convegence of Figure 4, it is divided to three parts; first part is from zero voltage to the lower turning point; the second part is from the lower turning point to the upper turning point, and the third part is from the upper turning point onwards. For the first part, convergence is achieved using the first two mode shapes. In the second part, conevergence happens for some parts using the first four modes. In the third part, convergence is obtained for the most part by using the first four modes. A three-mode-model though shows reasonable accuracy and will be used for determining multi-mode dynamic results in section 4.2.

Figure 5 also shows how the roots q_1 of Eq. (26) change as the voltage varies for different controller gain values in the complex plane. The results are shown for varying voltage between 0 and 150 V. Lowering the gains leads to an extension of the range of real roots. For example, for $G = 1$, the lowest gain in the figure, we have the maximum number of real roots on the real axis, or the maximum distance between the two loci of roots intersecting on the real axis.

Figure 5 also leads to an important conclusion. In Eq. (25) the only parameter that changes the coefficients of this equation is $G^2\alpha$. According to Eq. (6), changing the dimensions of the cantilever beam, alters α, but the product of $G^2\alpha$ is what changes the results of the Eq. (25) . Therefore, we can change the gain of the controller G to keep $G^2\alpha$ constant in order to get the same results for different beam dimensions. To demonstrate this observation, Figure 6 is plotted for a constant $G^2\alpha = 0.0002$, but for different controller gains, G and different α. As can be seen, they are identical. The dimensions that correspond to the chosen values of α are listed in Table 2.

The number of real roots in Figure 5 indicates bifurcations in the system. For gains higher than 5, there are always two complex roots and the locus of roots does not touch the real axis. For gains less than 3.5, the two complex branches intersect the real axis at two points meaning that we get two repeated real

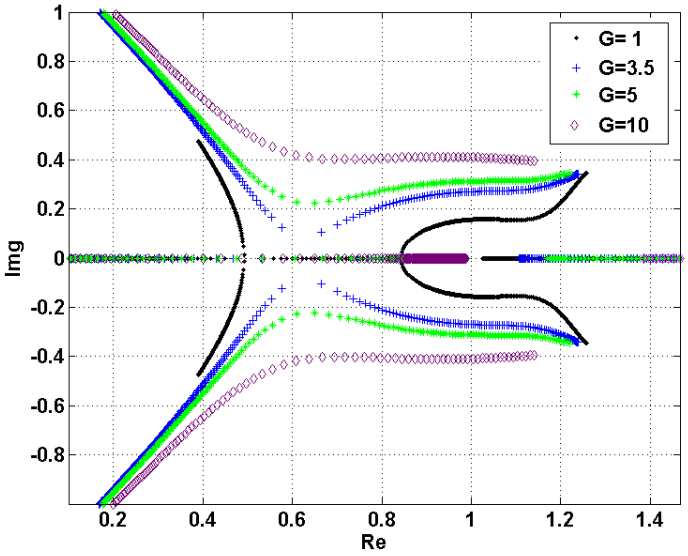

Figure 5: Eq. (26) roots, q_1 in complex plane for different controller gains.

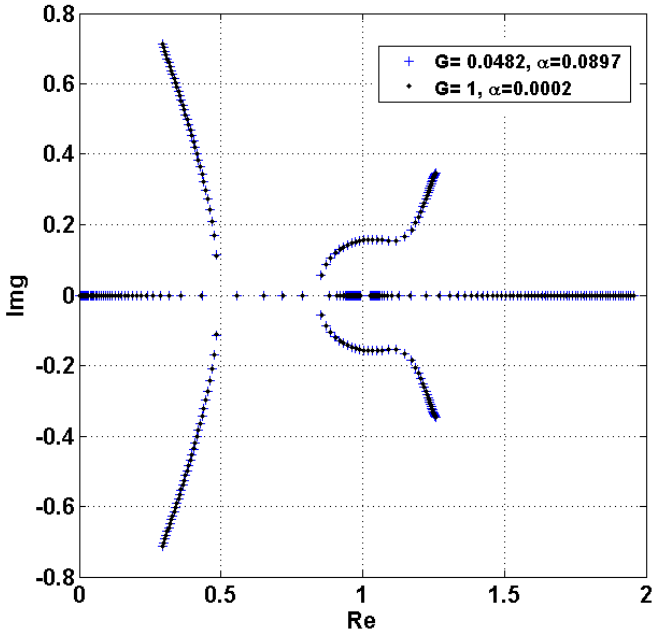

Figure 6: q_1 roots in complex plane for a constant $G^2\alpha = 0.0002$.

roots at each intersection, each corresponds to a different voltage. For a controller gain of about 3.5, the two complex branches meet at a single point on the real axis. That means the range for the unstable equilibrium point on the real axis disappears and the two loci of stable equilibrium points on the real axis at the right and left sides of the intersection join together. This point is a cusp

Table 2: Beam dimensions for the two cases shown in Figure 6.

α	$L(\mu m)$	$b(\mu m)$	$h(\mu m)$	$d(\mu m)$
0.0002	200	80	4.5	3
0.0897	496	10	2	3

point in the parameter space of voltage V and gain G, where we get a triple repeated root for q_1 at a unique voltage and gain. It is a codimension-2 bifurcation, meaning that we have to tune two parameters V and G to achieve this type of bifurcation. In order for the system to be bi-stable, the controller gain has to be less than the critical gain at the cusp point.

The effect of controller gain on the size of the bi-stability region is clearly depicted in Figure 7. As may be seen, there is a critical gain when the bi-stable region vanishes. In this case, the two turning points change to an inflection point for gains higher than about 3 in the figure. For gains less than 3, the bi-stable region exists, which for smaller gains, is wider and starts at a larger voltage.

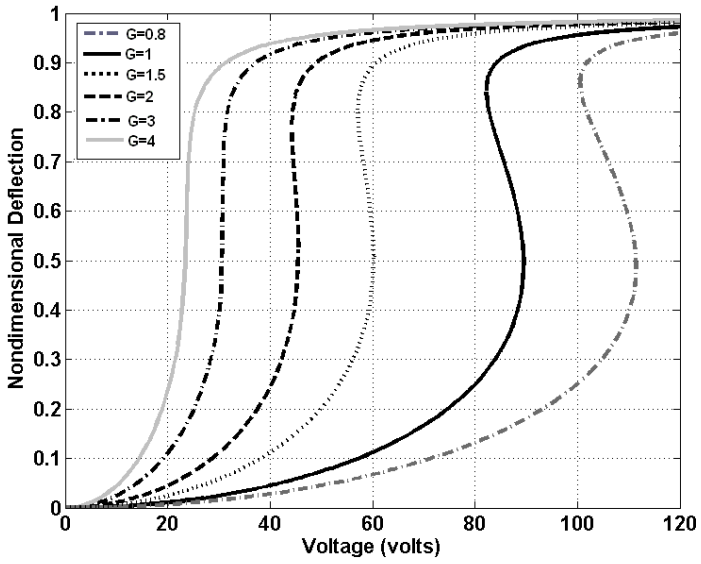

Figure 7: Effect of controller gain, G, on static pull-in graph for system parameters listed in Table 1.

To find the critical gain using a one mode approximation, the properties that should be satisfied are studied first. The treshold of bi-stability is when the Eq. (26) has a triple root or in other words, when it can be written as

$$F(q_1) = (q_1 - p_0)^3 \left(q_1^2 + p_1 q_1 + p_2\right) = 0 \qquad (28)$$

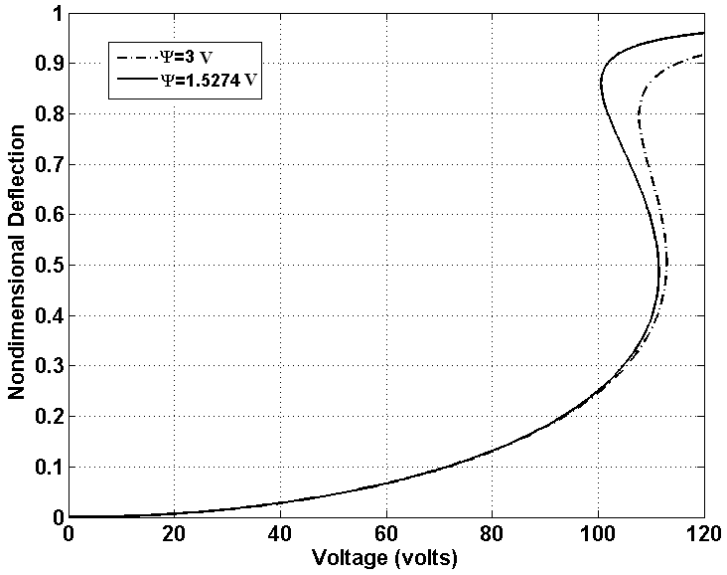

Figure 8: Effect of controller parameter,Ψ on static pull in graph for system parameters listed in Table 1 except that $G = 0.8$.

where p_0 is the triple root. Due to having a triple real root, the following can be concluded about the derivatives of Eq. (28):

$$\left.\frac{dF}{dq_1}\right|_{q_1=p_0} = 0 \tag{29}$$

and,

$$\left.\frac{d^2F}{dq_1^2}\right|_{q_1=p_0} = 0. \tag{30}$$

Solving Eqs. (28), (29), and (30) numerically resulted in the tuned parameters of the cusp point (V, G) and the triple real root of q_1. The critical parameters for the threshold of the bistability are found to be the critical gain $G_{cr} = 3.4705$, the citical voltage $V_{cr} = 26.965V$, and the nondimensional deflection $q_{cr} = 0.6256$.

Not only can the controller gain affect the bi-stability voltage range, but also the sensor system parameter Ψ or more sepcifically K_s, sensor amplfier gain, in Eq. (22), can affect the bi-stability voltage range as well as the bi-stability range of the deflection. According to Eq. (24), increasing Ψ decreases the magnitude of the right hand side of the equation which is proportional to the electrostatic force. In other words, in the equilibrium equation between electrostatic force and the spring force, increasing of Ψ lowers the magnitude of the electrostatic force, helping the spring force to bring the system back to equilibrium and avoid pull-in.

The effect of Ψ is demonstrated in Figure 8 using a one mode apprixiamation for the system based on the parameters in Table 1 except that here the controller gain is $G = 0.8$. Figure 8 shows that by increasing the sensor parameter, Ψ, one can push the static profile away from pull-in, which makes the system safer to operate. On the other hand, the disadvantage of increasing the Ψ is that the volatge range for the bi-stability region decreases from 9 V for $\Psi = 1.5274V$ to 4.5 V for $\Psi = 3V$. Therefore, by proper selection of controller gain, G and the sensor parameter Ψ one can adjust the bi-stable region as well as the deflection of the upper equilibrium point. By choosing $G = 0.8$ and $\Psi = 3V$, for the bi-stability region, we get a voltage range of 4.5 V, and the upper stable equilibruim is less than 0.9, which is far enough from pull-in and safe for operation. Therefore, from this point forward, the parameters of the system are based on Table 1, except that $G = 0.8$ and $\Psi = 3V$.

4 Dynamic Analysis

The stability of the fixed points will be examined and then the dynamic responses are presented using one- and three-mode-models. To analyze the dynamics after adding the controller, first the state space equations are derived. Derivation is performed by decretization of Eqs. (19) and (21) using Galerkin's method. Using the first mode approximation, the resulting two differential equations would be in terms of q_1, the normalized beam tip deflection for a single mode. Letting $y_1 = q_1$, $y_2 = \dot{q_1}$, and $y_3 = V_s$, the system state space equations become

$$\begin{cases} \dot{y_1} = y_2 \\ \dot{y_2} = \frac{-(\hat{c}_0+\hat{c}_1y_1+\hat{c}_2y_1^2+\hat{c}_3y_1^3)-y_2(\hat{c}_4+\hat{c}_5y_1+\hat{c}_6y_1^2)-G^2(V_r-y_3)^2}{\hat{c}_7+\hat{c}_8y_1+\hat{c}_9y_1^2} \\ \dot{y_3} = -r(y_3 - \frac{y_1}{1-y_1}\Psi\sqrt{\alpha}) \end{cases} \tag{31}$$

where $\hat{c}_0, \ldots, \hat{c}_9$ are the coefficents from Galerkin's method.

4.1 Stability of Fixed Points

In this section, the stability of the fixed points is discussed using a one mode approximation. To find the stability, Eq. (31) is linearized about the equilibrium points. For the equilibrium points,

$$y_3 = \frac{y_1}{1-y_1}\Psi\sqrt{\alpha}. \tag{32}$$

Equation (32) is used in Eq. (31) and the third order system is reduced to the second order system:

$$\begin{cases} \dot{y_1} = y_2 \\ \dot{y_2} = \frac{-(\hat{c}_0+\hat{c}_1y_1+\hat{c}_2y_1^2+\hat{c}_3y_1^3)-y_2(\hat{c}_4+\hat{c}_5y_1+\hat{c}_6y_1^2)-G^2(V_r-\frac{y_1}{1-y_1}\Psi\sqrt{\alpha})^2}{\hat{c}_7+\hat{c}_8y_1+\hat{c}_9y_1^2} \end{cases} \tag{33}$$

The linearized from of Eq. (33) is then written as

$$\dot{\mathbf{y}} = \mathbf{A}\mathbf{y} \tag{34}$$

where $\dot{\mathbf{y}} = \begin{bmatrix} \dot{y}_1 \\ \dot{y}_2 \end{bmatrix}$, $\mathbf{y} = \begin{bmatrix} y_1 \\ y_2 \end{bmatrix}$, and A is the Jacobian matrix:

$$A = \begin{bmatrix} 0 & 1 \\ f_1 & f_2 \end{bmatrix} \tag{35}$$

where

$$f_1 = \frac{\partial \dot{y}_2}{\partial y_1}, \quad \text{and} \quad f_2 = \frac{\partial \dot{y}_2}{\partial y_2} \tag{36}$$

Stability of the fixed points is investigated by finding the eigenvalues λ of the Jacobain matrix A, which is evaluated at the magnitude of the fixed points:

$$|\tilde{A} - \lambda I| = \lambda^2 - \tilde{f}_2\lambda - \tilde{f}_1 = \lambda^2 - \tau\lambda + \Delta = 0 \tag{37}$$

where $\tilde{A}, \tilde{f}_1$, and $\tilde{f}_2$ are evaluated at the fixed point and $\tau = \lambda_1 + \lambda_2$, and $\Delta = \lambda_1\lambda_2$.

To examine the stability of the fixed points in the bistable region, a specified volatge in this region is selected and the eigenvalues are calculated as well as Δ and τ. Table 3 shows the eigenvalues computed for the fixed points at $V = 110$ V for $G = 0.8$, and $\Psi = 3V$ (Figure 8). In Table 3 four roots(fixed points) and their corresponding eigenvalues are listed as one of the roots is greater than one and is non-physical. As can be seen in Table 3, the first fixed point corresponds to a stable spiral [9]; the second fixed point corresponds to a saddle point; the third fixed point is a stable spiral and the fourth fixed point is a saddle again. Therefore, there are two stable fixed points in this region that are accompanied by two unstable fixed points.

Table 3: Eigenvalues for the fixed points at $V = 110$ *Volts* in Figure 8 for $G = 0.8, \Psi = 3V$.

q_1	EV 1	EV 2	τ	Δ	$\tau^2 - 4\Delta$
0.37	-0.37 - 1.97i	-0.37 + 1.97i	-0.73	4.01	-15.51
0.68	1.60	-2.33	-0.73	-4.31	17.78
0.864	-0.37 - 4.45i	-0.37 + 4.45i	-0.73	19.95	-79.27
0.985	61.17	-61.90	-0.73	-3787	15148

Eigenvalues at the stable fixed points also reveal the magnitude of the oscillation frequency. In Table 3, the nondimensional circular frequency for the first and third fixed points are 1.97 and 4.45 respectively. Regarding the fact that the canonical circular frequencies for a cantilever beam is 3.5158, one can conclude that the natural frequency for the first stable equilibrium point is decreased by adding the controller and it is increased for the second stable equilibrium point. The mentioned frequencies also can be found at V=100 V in Figure 9, which shows the nondimensional circular frequency (imaginary parts of the eigenvalues) obtained for the lower(first) and upper(second) equilibrium points using a one mode approximation and linearization about those points at different voltages. There is a common voltage range for both fixed points in the figure, which represents the bistability region. In this range, starting about 108 V up to 112.5 V, the system has different natural frequencies for each equilibrium point. These frequencies will be used in section 4.2 for excitation of the system.

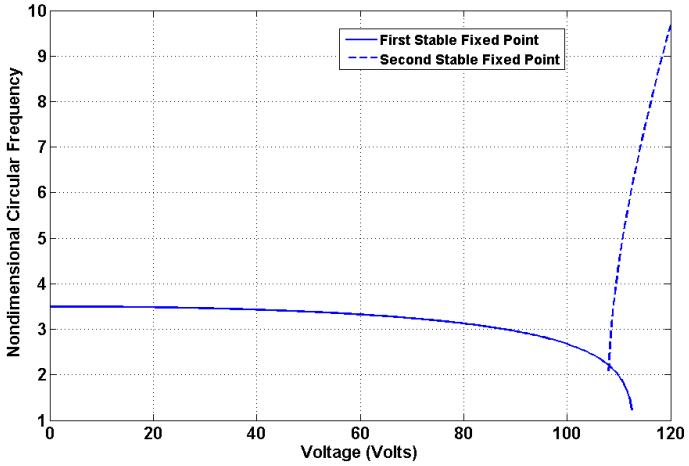

Figure 9: Nondimensional circular frequency versus voltage.

4.2 Dynamic Reponse Results

The dynamic response of the system with the controller in the bistability region is examined here using one- and three-mode-models. Starting with a one mode approximation, the solution to Eq. (31) is obtained numerically for different initial conditions and operating voltages. So far the voltage was assumed constant, but here for the dynamic analysis the reference voltage, V_{ref} in Eq. (20) has two parts including both DC and AC:

$$V_{ref} = V_{DC} + V_{AC}\cos(\omega t). \tag{38}$$

where ω is the nondimensional circular frequency of excitation, V_{AC}, and V_{DC} are the operating AC and DC voltages, respectively and t is the nondimensional time. Substituting Eq. (38) into Eq. (20) yields

$$V_r = \sqrt{\alpha}(V_{DC} + V_{AC}\cos(\omega t)). \tag{39}$$

Equation (39) is then substituted into Eq. (31) which is solved numerically for y_1, y_2, and y_3 for assumed initial conditions. It should be noted that for the simulations, the bandwidth r of the low pass filter used in the sensor has been changed from 1 in Table 1 to 100 because of the high frequency system here in comparison to the system used in [6]. Therefore, the bandwidth has been increased to catch the entire range of oscillations.

To verify the program for dynamic solution, free vibration is first examined. That is, an operating DC voltage in the bi-stability region from Figure 8 is chosen, for example $V_{DC} = 110\ V$ for $\Psi = 3$ V and then the solution is sought using initial condition in the neighbourhood of the two equilibrium points. Figures 10 and 11 show the convergence of the dynamic solution to the static solution in the nondimensional phase portrait and time series of displacement and sensor output voltage in the absence of AC voltage. Because of sufficient damping in the system, the vibrations damp out to the upper stable equilibrium points at 0.864 and to the lower stable equilibrium at 0.37, respectively. The normalized sensor output voltage (V_s) also settles down at 0.275 and 0.026, that can be calculated from Eq. (23) for $w_1 = 0.86$ and $w_1 = 0.37$, respectively. The dimensional sensor output voltage is found from dividing by $\sqrt{\alpha} = 0.014$ (Eq.23) and thus in the above case, the settled voltages are 19.1 V and 1.8 V, respectively.

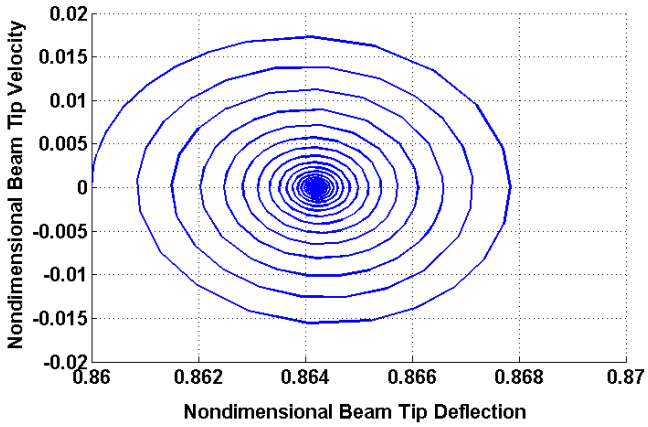

Figure 10: Convergence to the upper equilibrium point for system parameters of $G = 0.8$, $\Psi = 3$, $r = 100$, $\mu = 0.7$, $\omega = 3.5158$, $V_{AC} = 0$ V, $V_{DC} = 110$ V and initial condition of ($q_1 = 0.86,\ \dot{q}_1 = 0,\ V_s = 0.266$).

Figures 12 and 13 demonstrate the dynamic response of the system in the bi-stability region with the operating voltage, $V_{DC} = 110$ V and V_{AC} of 0.7 V and 0.9 V, respectively starting from an initial condition in the vicinity of the upper equilibrium point. Figure 12 shows the egg shape of limit cycle formed around the second equilibrium point with applying V_{AC} of 0.7

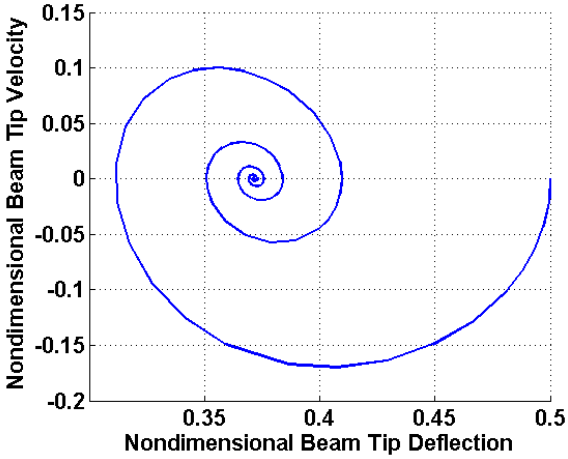

Figure 11: Convergence to the lower equilibrium point for system parameters of $G = 0.8$, $\Psi = 3$, $r = 100$, $\mu = 0.7$, $\omega = 3.5158$, $V_{AC} = 0$ V, $V_{DC} = 110$ V and initial condition of ($q_1 = 0.5,\ \dot{q}_1 = 0,\ V_s = 0.04$).

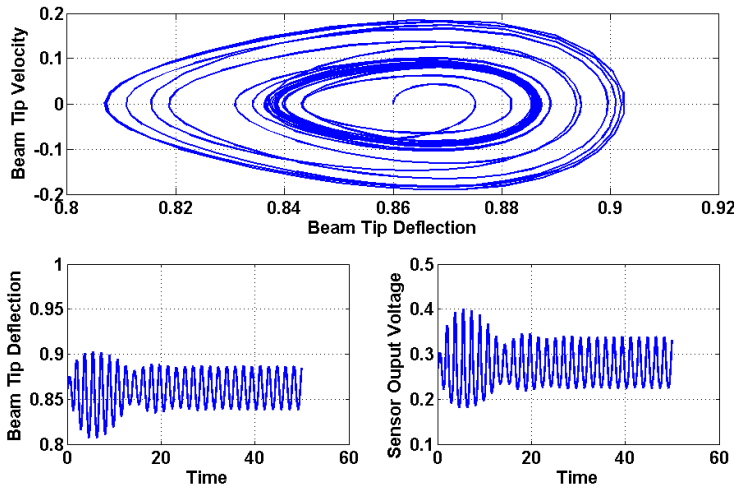

Figure 12: The nondimensional phase plane,beam deflection and sensor output voltage(Volts) for system parameters of $G = 0.8$, $\Psi = 3$, $r = 100$, $\mu = 0.7$, $\omega = 3.5158$, $V_{AC} = 0.7\ Volts$, $V_{DC} = 110 Volts$ and initial condition of (0.86,0,0.266).

V. Figure 13 shows the basin of attraction for the second stable equilibrium point. It also clearly depicts the bistability characteristic of the system by adding the controller. As the operating AC voltage is increased from 0.7 V in Figure 12 to 0.9 V in Figure 13, we see the escpae from the upper potential well to the lower potential well and the motion ends in a periodic oscillation in the lower well (small limit cycle about the first equilibrium point). It is noted that the foramtion of the limit cycle is because of forcing (V_{AC}), otherwise it would merge into the equilibrium point. By increasing the AC voltage, it has been found that the lower

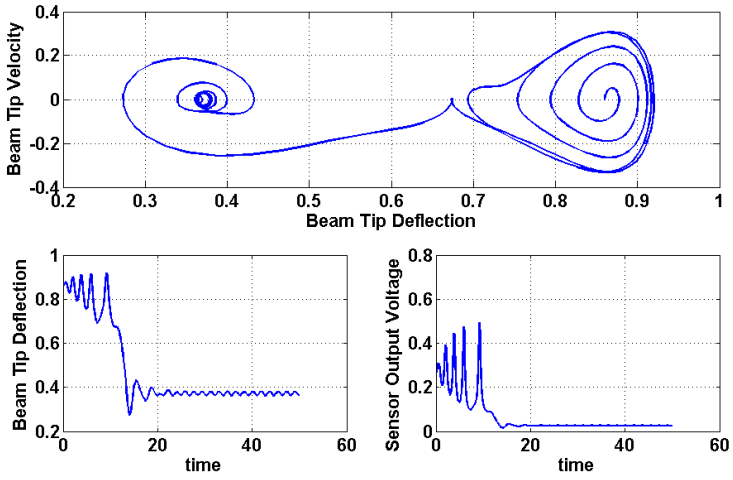

Figure 13: The nondimensional phase plane,beam deflection and sensor output voltage(Volts) for system parameters of $G = 0.8$, $\Psi = 3$, $r = 100$, $\mu = 0.7$, $\omega = 3.5158$, $V_{AC} = 0.9$ *Volts*, $V_{DC} = 110$*Volts* and initial condition of ($q_1 = 0.86$, $\dot{q}_1 = 0$, $V_s = 0.266$).

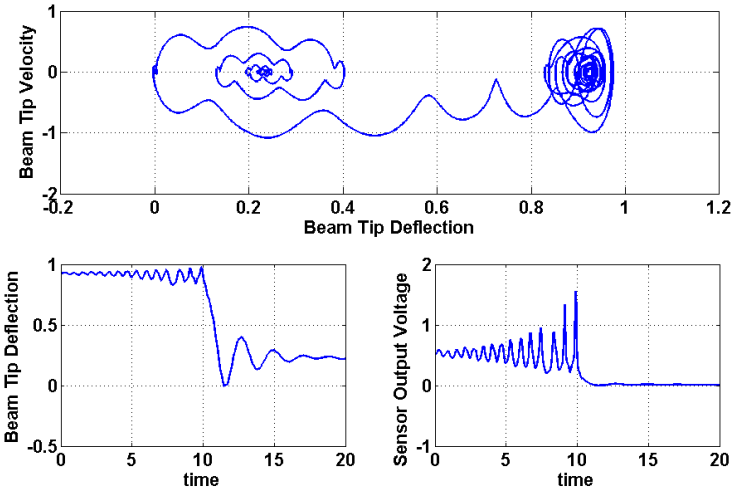

Figure 14: The nondimensional phase plane,beam deflection and sensor output voltage(Volts) for three modes and for system parameters of $G = 0.8$, $\Psi = 3$, $r = 100$, $\mu = 0.7$, $\omega = 2.8$, $V_{AC} = 0.9$ V, V_{DC}=100 V, and initial condition of ($q_1 = 0.86$, $\dot{q}_1 = 0$, $V_s = 0.266$).

potential well is much deeper than the upper well, and when the energy reaches a threshold so that the escape happens from the upper well to the lower one, it never comes back and it keeps oscillating in the lower well. Therefore, to get chaos, it seems that the depth of potentail wells should be adjusted to get equally deep wells.

Using three-mode-model, Figure 14 shows the forced oscillation of the system when a DC voltage, V_{DC} in the bi-stability region for three-mode-model is applied (e.g. 100 V) along with

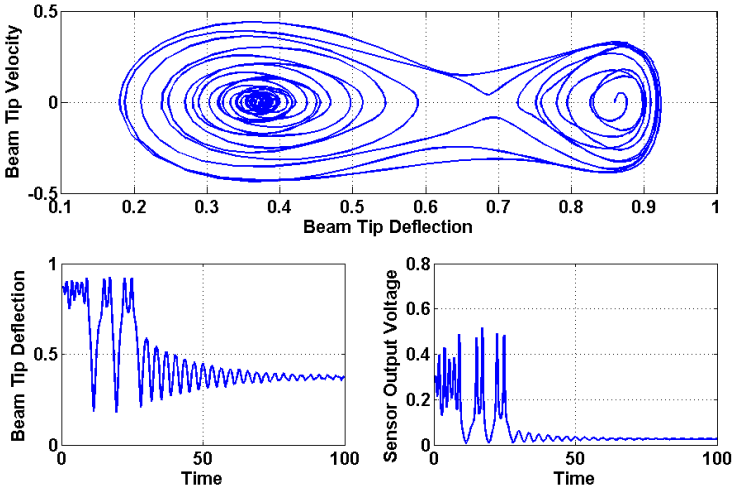

Figure 15: The nondimensional phase plane,beam deflection and sensor output voltage(Volts) for system parameters of $G = 0.8$, $\Psi = 3$, $r = 100$, $\mu = 0.1$, $\omega = 4.45$, $V_{AC} = 0.86$ *Volts*, $V_{DC} = 110$*Volts* and initial condition of ($q_1 = 0.86$, $\dot{q}_1 = 0$, $V_s = 0.266$).

a small AC voltage of 0.9 V. The trajectory starts from an initial condition close to the upper fixed point, and it escapes to the lower fixed point and then is attracted to a small limit cycle around it. The curly shape in the phase plane reveals the characteristic of multi-mode-model which has multiple frequencies.

To demonstrate the basins of attarction more clearly, Figure 15 is drawn. The basins around two stable fixed points and the saddle node are clearly shown. In the simulations, the damping of the system has been reduced from 0.7 to 0.1 for the results shown, although in a physical system, we do not have much control over damping. As it is seen in the figure, the motion starts around the upper equilibrium; it grows; by the saddle in the middle, it is thrown to circle both equilibriums and becoming closer to the highly stabilized lower fixed point, it ends in small periodic oscillations around it.

Our results show that we are close to creating chaos by tuning the system paramters so that instead of having one dominant stable fixed point, we get two almost equally stable fixed points that lead us to a consistent exchange of energy between the two potential wells without being trapped in one well. The above statement is for the case when chaos is desired between the two wells. However, seeking chaos in one potential well is also sought in the future which can be obtained by tuning the amplitude and frequency of forcing.

5 Conclusions

Research on MEMS actuators and sensors, which are looking for more efficiency and sensitivity is increasing. In this paper, we simulate the deflection of a micro cantilever beam in an elec-

trostatic field using a multi-degree-of-freedom model, which is shown to be a more accurate model than a lumped mass spring damper system mostly used in the literature. We found that pull-in happens at 45 percent of the initial gap for the cantilever beam, which is larger than the 33 percent reported so far for lumped-mass models.

The micro-actuator with one stable equilibrium point has been converted to a bi-stable system using a controller proposed by Liu [6]. In the work by Liu [6], they could obtain only the hystersic profile or the stable parts of the static profile using a lumped mass model, while we have obtained the static response of the beam with the controller showing both stable and unstable branches. The effect of the controller on the static response has been studied for a multi-degree-of-freedom model of the catilever beam rather than a lumped parameters system. We also discussed the number of modes required to get convergence for the system with and without the controller. In addition, the effect of system parameters on the bi-stability properties have been studied. We found that the decreasing the controller gain can increase the range of voltage, for which we can have bi-stability. Increasing of sensor amplification factor has also been found effective in lowering down the upper equilibrium point which is desired in most electrostatic actuators.

In addition to static profiles, we have produced dynamic responses of the system at the operating voltages where the system becomes bi-stable. Not only the basins of attraction of the two fixed points are demonstreted but also we have shown the exchange of energy between the wells of potential field. The goal of having a bi-stable actuator is creating chaos; tuning the parameters of the system to balance the forcing and damping that makes the beam oscillate around one equilbrium point and then the other in a random manner. Beside creating chaos between the two fixed points, as future work we seek to create chaos in one well and we will use the other potential well to protect it from pull-in.

REFERENCES

[1] J. Bienstman, J. Vandewalle, R. Puers, "Autonomous impact resonator: A new operating principle for a silicon resonant strain gauge", *Sensors and Actuators*, A: Physical, v 66, n 1-3, pp 40-49, 1998.

[2] Y. C. Wang, S. G. Adams, J.S. Thorp, N. C. MacDonald, P. Hartwell, F. Bertsch, "Chaos in MEMS, parameter estimation and its potential application", *IEEE Transactions on Circuits and Systems I: Fundamental Theory and Applications*, v 45, n 10, pp 1013–1020, 1998.

[3] A. Raman, S. Hu, "Chaos in dynamic atomic force microscopy",*2006 International Symposium on Nonlinear Theory and its Applications*, pp 911–14, Bologna, Italy, 11-14 Sept. 2006.

[4] Y. Zhang, Y. Zhao, "Numerical and analytical study on the pull-in instability of micro-structure under electrostatic loading", *Sensors and Actuators A (Physical)*, v 127, n 2, pp 366–80, 2006.

[5] A. C. J. Luo, F. Y. Wang, "Chaotic motion in a micro-electro-mechanical system with non-linearity from capacitors", *Communications in Nonlinear Science and Numerical Simulation*, v 7, n 1-2, pp 31–49, 2002.

[6] S. Liu, S. , A. Davidson, Q. Lin, "Simulation studies on nonlinear dynamics and chaos in a MEMS cantilever control system", *Journal of Micromechanics and Microengineering*, v 14, n 7, pp 1064-1073, 2004.

[7] M. I. Younis, E.M. Abdel-Rahman, A. Nayfeh, "A reduced–order model for electrically actuated microbeam-based MEMS", *Journal of Microelectromechanical Systems*, v 12, n 5, pp 672–680, October 2003.

[8] S.S. Rao, *Mechanical vibrations*, Pearson Prentice Hall, N.J., 4th ed., 2004.

[9] S. H. Strogatz, *Nonlinear dynamics and Chaos : with applications in physics, biology, chemistry, and engineering*, Westview Press, 1994, USA.